# nature synthesis

**Article** 

https://doi.org/10.1038/s44160-024-00597-3

# Interdiffusion-enhanced cation exchange for HgSe and HgCdSe nanocrystals with infrared bandgaps

Received: 8 February 2024

Accepted: 6 June 2024

Check for updates

Wonseok Lee © 1,2 & Andrew M. Smith © 1,2,3,4,5,6

Colloidal semiconductor nanocrystals based on CdSe have been precisely optimized for photonic applications in the visible spectrum, with modern products exhibiting structural uniformity, near 100% quantum yield and linewidths narrower than 100 meV. Here we report homogeneous nanocrystals with tunable bandgaps in the infrared spectrum based on HgSe and Hg<sub>x</sub>Cd<sub>1-x</sub>Se alloys deriving from CdSe precursors. We find that Ag<sup>+</sup> catalyses cation interdiffusion to reduce the CdSe-HgSe alloying temperature from 250 °C to 80 °C. Together with ligands that modulate surface cation exchange rates, interdiffusion-enhanced Hg<sup>2+</sup> exchange of diverse CdSe nanocrystals proceeds homogeneously and completely. The products retain the size, shape and uniformity of the parent nanocrystals but exhibit enhanced absorption. After passivation with heteroepitaxial CdZnS shells, photoluminescence wavelengths are tunable in the shortwave infrared by composition without changing size, with 80-91% quantum yield and linewidths near 100 meV. These materials may find applications in infrared photonic devices and infrared bioimaging.

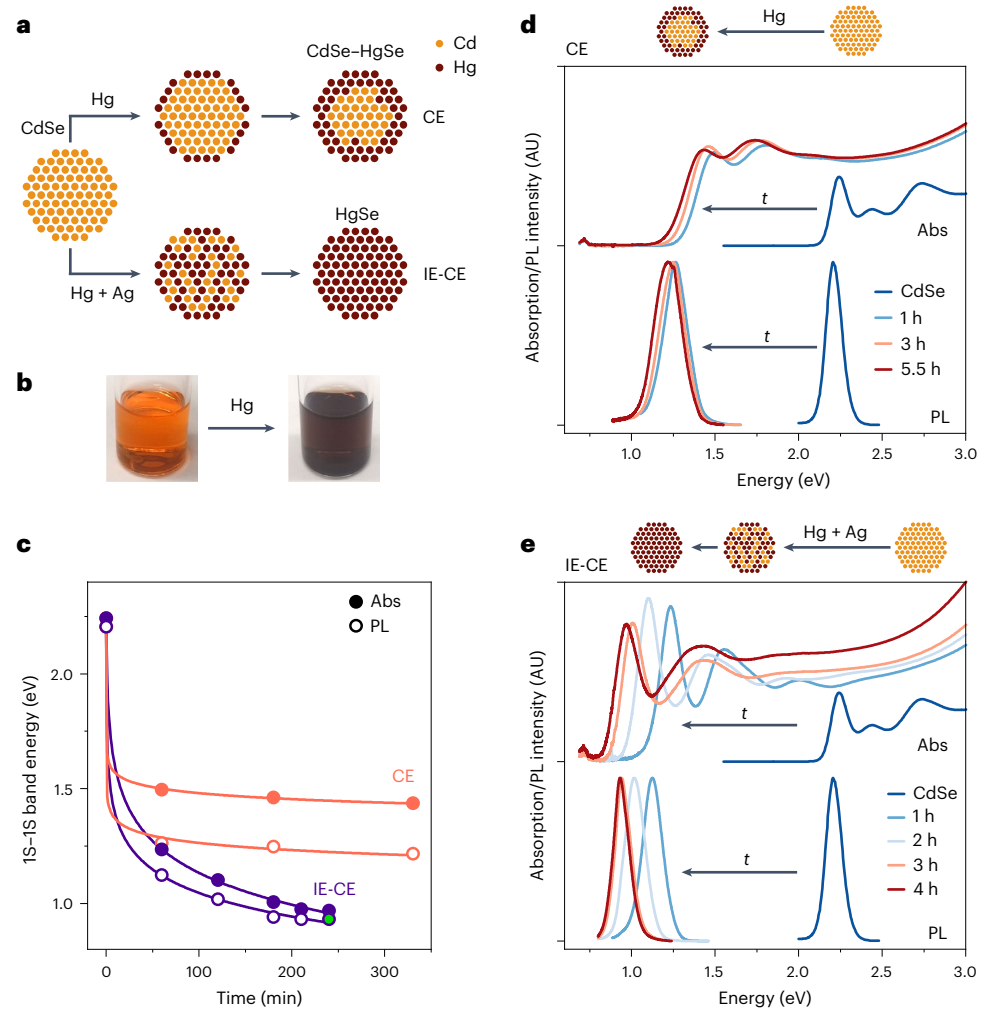


Colloidal semiconductor nanocrystals (NCs) are solution-dispersed, solution-processed nanomaterials that provide a unique combination of photophysical properties for applications in photonic devices and bioimaging. With these materials, electronic energy levels and optical bandgaps are tunable by both size and composition with large absorbance cross sections, high photoluminescence (PL) quantum yield (QY) and long-term photochemical and photophysical stability<sup>1</sup>. Following the first syntheses of monodispersed and size-tunable cadmium chalcogenide NCs in 1993 (ref. 2), considerable developments have been made towards NCs with controllable shapes, crystal structures, compositional heterostructures and surface facets<sup>3</sup>. This structural control together with predictive models of quantized energy levels now allows the precise design of electronic transitions, dynamics and charge interactions<sup>4</sup>. Visible spectrum NCs, especially prototypical CdSe NCs and their core–shell CdSe–CdZnS heterostructures, now

are widely used light emitters with PL QY near 100%, bandwidths near 100 meV and size distributions near 5% (refs. 5,6).

NCs with optical bandgap energies in the infrared spectrum are being pursued for applications in infrared photonic devices and deep-tissue bioimaging<sup>7,8</sup>. The most developed binary NC materials with infrared bandgaps include InAs, PbS, PbSe, HgSe and HgTe, all of which are less advanced compared with their counterparts in the visible spectrum owing to distinct challenges in synthesis. III–V InAs NCs are challenging to prepare with homogeneous sizes, especially for larger sizes with narrower bandgaps, while PL QY is limited by interfacial defects at heterovalent interfaces incorporating insulating II–VI shell compounds such as CdSe, CdS and ZnS<sup>9,10</sup>. IV–VI PbS and PbSe NCs can be synthesized with tunable bandgaps across a wide range of sizes with high monodispersity<sup>11,12</sup>, but shell deposition required to prevent oxidation<sup>13,14</sup> broadens linewidths due to lattice mismatch with

<sup>1</sup>Department of Bioengineering, University of Illinois Urbana-Champaign, Urbana, IL, USA. <sup>2</sup>Micro and Nanotechnology Laboratory, University of Illinois Urbana-Champaign, Urbana, IL, USA. <sup>3</sup>Carl R. Woese Institute for Genomic Biology, University of Illinois Urbana-Champaign, Urbana, IL, USA. <sup>4</sup>Department of Materials Science and Engineering, University of Illinois Urbana-Champaign, Urbana, IL, USA. <sup>5</sup>Cancer Center at Illinois, University of Illinois Urbana-Champaign, Urbana, IL, USA. <sup>6</sup>Carle Illinois College of Medicine, Urbana, IL, USA. ⊠e-mail: smi@illinois.edu



 $\label{eq:Fig.1} \textbf{Fig. 1} | \textbf{IE-CE of CdSe NCs with Hg}^{2^+}. \textbf{a}, \textbf{S} chematic representation of CdSe NC exchange using either Hg}^{2^+} alone (CE) or in combination with Ag^+ (IE-CE), generating either core–shell CdSe–HgSe NCs or homogeneous alloy Hg_xCd_{1-x}Se NC alloys, respectively. IE-CE proceeds to yield binary HgSe NCs.$  $<math display="block">\textbf{b}, \textbf{P} hotographs showing CdSe NC solution before and 5 s after the addition of Hg^{2^+} at room temperature. \textbf{c}, The time course of spectral IS-IS band energies for CE (orange) and IE-CE (purple), showing absorption (Abs) and PL. After 4 h of$ 

IE-CE (green-filled purple circle), the exchange of  $Cd^{2+}$  with  $Hg^{2+}$  is nearly complete (Supplementary Table 2).  $\mathbf{d}$ , Absorption and PL spectra of 3.3 nm NCs during CE at 80 °C. The spectra are plotted in arbitrary units (AU), with absorption spectra normalized by NC concentration and PL spectra normalized by maximum intensity.  $\mathbf{e}$ , Absorption and PL spectra during IE-CE at 80 °C. The spectra are normalized as in  $\mathbf{d}$ .

II-VI shell materials and heterogeneity of shell thickness. In contrast, II–VI HgSe and HgTe NCs have homovalence and equivalent cubic zinc blende crystal structures as canonical II-VI CdS and ZnS shells that should enable homogeneous and low-defect core-shell heterostructures with high PL QY and flexible optical tunability through the HgSe or HgTe core size<sup>15,16</sup>. Nevertheless, telluride-based NCs have a propensity to oxidize even with shells, and synthetic challenges remain for HgSe NCs. Syntheses and processing of mercury chalcogenide NCs require low temperatures (typically 0-120 °C) to avoid NC degradation and  $reduction \, of \, Hg^{2^+} precursors \, (Supplementary \, Table \, 1). \, This \, contrasts$ with other II-VI materials that are stable at high temperatures (typically 200–380 °C) and compatible with coordinating ligands with diverse hard and soft basic groups such as carboxylates, amines and phosphonates. As a result, current HgSe NCs have wide size distributions (near 10-20% (refs. 17-19)) and their maturity in terms of size, shape and heterostructure engineering lags well behind visible semiconductor NCs based on CdSe.

HgSe can alloy with CdSe to form ternary  $Hg_xCd_{1-x}Se$  alloys with wide, continuous tunability of photophysical properties, including bandgaps spanning 1.74 eV (CdSe) to -0.06 eV (HgSe), comprising the entire infrared spectrum<sup>15</sup>. Moreover, the lattice mismatch between

CdSe and HgSe is smaller than 0.5% ( $a_{\text{CdSe}} = 6.05 \text{ Å}$ ,  $a_{\text{HgSe}} = 6.08 \text{ Å}$ ) such that there is only a small dependence of materials properties on composition<sup>15</sup>. These properties mirror those of  $\text{Hg}_x\text{Cd}_{1-x}\text{Te}$ , which is the most common photonic material for high-performance infrared photodetectors as thin films and bulk materials owing to strong infrared absorption<sup>20</sup>. Alloys further allow tunability of photophysical and electronic properties through composition, independently of NC size, a key design characteristic for modern applications in multispectral bioimaging<sup>21</sup>. However, while composition-tunable ternary II–VI NCs can be readily prepared with diverse compositions (such as  $\text{Cd}_x\text{Zn}_{1-x}\text{Se}$ ,  $\text{CdSe}_x\text{S}_{1-x}$  and  $\text{CdSe}_x\text{Te}_{1-x}$ ), homogeneous  $\text{Hg}_x\text{Cd}_{1-x}\text{Se}$  NCs cannot be prepared using standard methods owing to disparate reaction temperatures required for mercury and cadmium precursors.

Cation exchange (CE) reactions allow the creation of ionic NCs that cannot be readily synthesized from elemental precursors by exchanging 'host' cations of pre-formed NCs with 'guest' cations, with the products inheriting the structural framework and distribution of the parent NCs. Through CE, guest compositional domains form within the parent NC through different pathways depending on the crystal structures and lattice parameters of the parent and product NC $^{22}$ . When crystal structures are equivalent, CE reactions typically proceed through a

**Fig. 2** | **Photophysical and structural characterization of binary HgSe NCs derived from IE-CE of CdSe NCs. a**, Absorption and PL spectra of a size series of CdSe NCs (yellow) and their IE-CE-derived HgSe NCs (brown). The PL spectra are shown in a dimmer shade. All spectra are normalized by their maximum intensity values. Band energy and PL FWHM values are tabulated in Supplementary Table 4. The sizes refer to the measured mean diameters of CdSe NCs.

**b**–**e**, Characterizations of 2.7 nm CdSe NCs and their IE-CE-derived HgSe NCs products show X-ray diffraction patterns with vertical lines indicating bulk zinc blende (ZB) diffraction patterns (**b**), size histograms with mean and relative standard deviation (s.d.) of diameter (**c**) and transmission electron micrographs (**d** and **e**). Scale bars, 10 nm.

core–shell intermediate with a shell rich in guest cations, as the surface exchange rate is much faster than the rate of interdiffusion between cations within the NC $^{23-25}$ . This is the case for the reaction between CdSe NCs and Hg $^{2+}$  cations which spontaneously displace Cd $^{2+}$  cations to generate core–shell CdSe–HgSe NCs $^{26}$ . With the exception of very thin CdSe nanoplatelets (NPLs), these CE reactions do not approach completion to yield binary HgSe $^{27}$ , as the Hg $^{2+}$ –Cd $^{2+}$  interdiffusion rate is much slower in CdSe domains forming the core compared with the HgSe shell domains, effectively trapping host cations within the NC at temperatures well below the CdSe–HgSe alloying temperature (-250 °C) $^{28}$ . The resulting CdSe–HgSe NCs have inferior optical properties. Homogeneous alloying through ion exchange reactions is rarely observed except in the case of perovskite anions $^{24}$ .

Here, we report interdiffusion-enhanced cation exchange (IE-CE) to generate homogeneous  $Hg_xCd_{1-x}Se$  alloy NCs and binary HgSe NCs (Fig. 1a). The cation interdiffusion rate is boosted by several orders of magnitude using a monovalent silver dopant, while the intrinsically rapid surface exchange rate is tuned using alkylthiol ligands. Reactions occur at low temperatures (80 °C) that yield stable colloidal products. We characterize the reaction process using chemical, physical and optical methods to understand the reaction mechanism and compare the photophysical figures of merit relative to products of standard CE. We further grow insulating shells on the NC products towards generating high-QY and narrow-band emission at shortwave infrared (SWIR) wavelengths (photon wavelengths 1,000–1,700 nm or energies 1.24–0.73 eV).

# **Results and discussion**

#### Complete CE with interdiffusion enhancer

In prototypical CE and IE-CE reactions, quasi-spherical CdSe NCs with 3.3 nm diameter and zinc blende crystal structure were dispersed in a solution containing alkylthiol and alkylamine ligands at 80 °C and treated with one of two reagents:  $Hg^{2+}$  alone or a mixture of  $Hg^{2+}$  and  $Ag^{+}$  (Hg+Ag). The colour of the NC solution changed from orange-red to black immediately after the addition of either reagent (Fig. 1b), indicating rapid replacement of a large fraction of  $Cd^{2+}$  with  $Hg^{2+}$  in the NC. The reaction proceeded to a greater extent with the Hg+Ag reagent. After 1 h with the Hg reagent, the lowest energy absorption band (1S–1S band transition) reduced in energy by 0.74 eV (from 2.24 eV to 1.50 eV) (Fig. 1c,d), whereas the Hg+Ag reagent induced a larger reduction of 1.00 eV (to 1.24 eV; Fig. 1c,e), consistent with a reduction in the

electronic bandgap. The emission band energy similarly decreased, with the Hg+Ag reagent yielding a shift from 2.21 eV in the middle of the visible spectrum to 1.13 eV in the SWIR. Conversion to HgSe was nearly complete in -4 h with the Hg+Ag reagent by elemental analysis (Supplementary Table 2). With the Hg reagent, exchange remained incomplete even after >48 h (Supplementary Table 3) and could not be accelerated by further heating due to NC ripening and flocculation above 100 °C (Supplementary Fig. 1)<sup>29,30</sup>.

A size series of CdSe NCs (2.3-4.0 nm) completely converted to HgSe NCs after several hours of reaction with the Hg+Ag reagent (Fig. 2a and Supplementary Fig. 2), retaining both crystal structure (Fig. 2b) and uniform sizes (~6% relative standard deviation of diameter; Fig. 2c-e and Supplementary Fig. 3). Consistent with the greater degree of quantum confinement in HgSe, the HgSe NC 1S-1S transition was enhanced ~2.6-fold compared with the CdSe NCs and the dependence of spectral band energy on size was greater for HgSe across this size range (Supplementary Fig. 4). The absorbance of HgSe NCs at 400 nm wavelength (3.1 eV) was proportional to the cube of diameter as  $0.0317d^3 \text{ cm}^{-1} \mu \text{M}^{-1}$ (where d is the NC diameter), which is larger than that of other narrow bandgap semiconductor NCs including PbS (0.0233d<sup>3</sup> cm<sup>-1</sup> μM<sup>-1</sup>)<sup>31</sup> and PbSe (0.0277d<sup>3</sup> cm<sup>-1</sup> μM<sup>-1</sup>)<sup>32</sup> (Supplementary Fig. 5) and greater than that of the parent CdSe NCs  $(0.0119d^3 \text{ cm}^{-1} \mu \text{M}^{-1} \text{ for } 3.4 \text{ nm CdSe})$ NCs). Strong absorbance at infrared wavelengths near the band edge as well as at higher energies are critical figures of merit for applications in infrared photovoltaics, photodetectors and PL applications<sup>33,34</sup>.

#### Dependence of absorption spectra on exchange mechanism

Spectral features in Fig. 1d,e indicate that the intermediate products of CE are core–shell CdSe–HgSe NCs, while the IE-CE intermediates are homogeneously alloyed Hg\_xCd\_1-xSe NCs. Absorption spectra of intermediates with equivalent PL band energies collected during the reactions are superimposed in Fig. 3a and deconvolved into individual transitions in Fig. 3b–d. The shapes of the absorption spectra of the CdSe NC and the IE-CE intermediate are similar, whereas there is a 67% reduction in the intensity of the 1S–1S transition in the CE intermediate. Carrier wavefunctions simulated by the effective mass approximation (EMA; Fig. 3e,f) indicate that, for both CdSe and Hg\_xCd\_1-xSe NCs, electron and hole wavefunctions strongly overlap across the NC, whereas for CdSe–HgSe NCs, a pseudo-type II band alignment is formed in which electrons are localized in the shell, while holes are delocalized throughout the NC. For CdSe–HgSe NCs the electron–hole overlap decreases

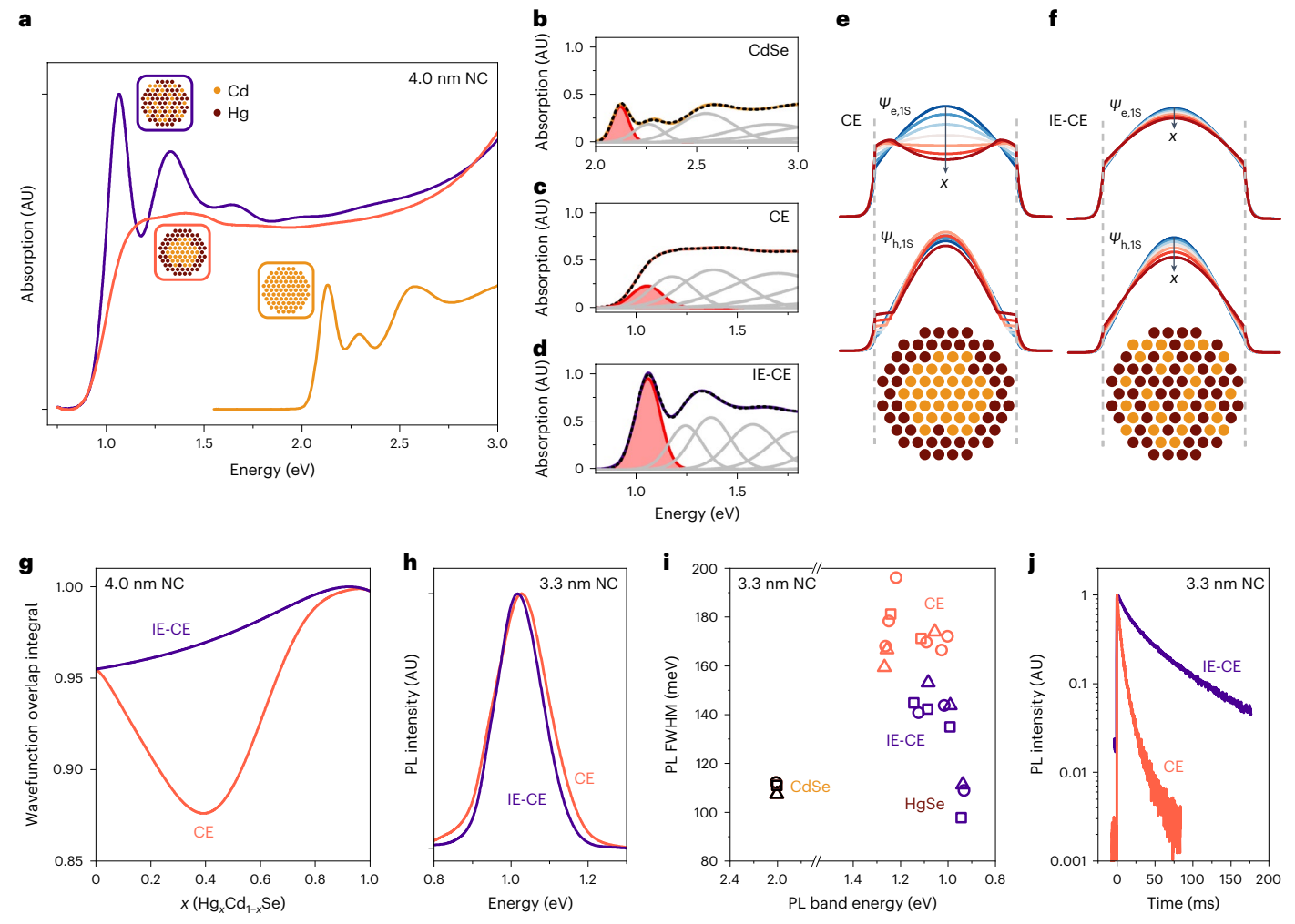


Fig. 3 | Dependence of photophysical properties on  $\operatorname{Hg}^{2+}$  exchange mechanism in CdSe. a, Absorption spectra of 4 nm CdSe NCs (yellow), CdSe–HgSe NCs produced by CE (orange) and  $\operatorname{Hg}_x\operatorname{Cd}_{1-x}\operatorname{Se}$  NCs produced by IE-CE (purple). The spectra are plotted in arbitrary units (AU) and normalized by NC concentration.  $\mathbf{b}$ – $\mathbf{d}$ , Absorption spectra in  $\mathbf{a}$  reconstructed as a sum of Gaussian functions (dotted black lines) reflecting individual electronic transitions (grey lines). Filled red curves indicate IS−1S band transitions.  $\mathbf{e}$ ,  $\mathbf{f}$ , EMA calculations of electron and hole wavefunctions of 4 nm NCs with total mercury composition of  $0 \le x \le 0.6$  for CdSe−HgSe NCs ( $\mathbf{e}$ ) and  $\operatorname{Hg}_x\operatorname{Cd}_{1-x}\operatorname{Se}\operatorname{NCs}$  ( $\mathbf{f}$ ). In CdSe−HgSe coreshell NCs, electron wavefunction is localized to the shell.  $\mathbf{g}$ , Wavefunction overlap

integrals of 4.0 nm CdSe–HgSe NCs and Hg<sub>x</sub>Cd<sub>1-x</sub>Se NCs calculated by the EMA. **h**, PL spectra of CdSe–HgSe NCs and Hg<sub>x</sub>Cd<sub>1-x</sub>Se NCs with similar PL band energies. Both NCs were generated from 3.3 nm CdSe NCs. Spectra are normalized by maximum intensities. **i**, PL FWHM of NCs showing data from three replicate CE and IE-CE reactions using 3.3 nm CdSe NCs. **j**, PL decay of 3.3 nm CdSe–HgSe NCs and Hg<sub>x</sub>Cd<sub>1-x</sub>Se NCs from **h**. Intensity trends fit well to two-component exponential decays as  $A_1 \exp(-t/\tau_1) + A_2 \exp(-t/\tau_2)$  with  $A_1 = 83.5\%$ ,  $\tau_1 = 3.8$  ns,  $A_2 = 16.5\%$ ,  $\tau_2 = 14.2$  ns for CdSe–HgSe NCs, and  $A_1 = 55.9\%$ ,  $\tau_1 = 18.8$  ns,  $A_2 = 44.1\%$ ,  $\tau_2 = 67.8$  ns for Hg<sub>x</sub>Cd<sub>1-x</sub>Se NCs.

with increasing mercury content (x) for compositions up to x = 0.4, which explains the reduction in 1S-1S transition strength (Fig. 3g). An increase in size from 2.3 nm to 4.0 nm enhances this charge separation, depleting up to 67% of the 1S-1S transition oscillator strength (Supplementary Fig. 6). For CdSe-HgSe NCs, there is also a substantial bowing of the 1S-1S band energy relative to the total composition x deriving from changes in the electron wavefunction shape and spatial delocalization (Supplementary Fig. 7). In contrast, for Hg<sub>x</sub>Cd<sub>1-x</sub>Se NCs, both EMA calculations and empirical results show a more linear relationship between composition and both the 1S-1S transition oscillator strength (Fig. 3g) and the 1S-1S band energy (Supplementary Fig. 7). These spectral differences with x are the best evidence for internal structure as the small sizes and spherical shapes of these NCs are not suitable for compositional mapping by scanning electron microscopy techniques. Previously, compositional contrast was possible using core-shell CdSe-HgSe nanoplatelets deriving from CE reactions that were vertically oriented on a substrate<sup>35</sup>. These results showed that two monolayers (MLs) of surface ions exchanged to HgSe on a CdSe

nanoplatelet core, which matches well to the maximum two ML depth of exchange that we calculate by EMA for CE reactions on spherical CdSe NCs (Supplementary Fig. 7).

# Dependence of PL on exchange mechanism

During the CE reaction, the PL full width at half maximum (FWHM) broadens relative to the CdSe NCs (Fig. 3h,i). The CE products consistently exhibited broader FWHM (-167–196 meV) than those of IE-CE (-109–143 meV). These wider bandwidths for CE products are similar to those of previous CdSe–HgSe NCs<sup>29,36</sup> and CdSe-based cores with epitaxial HgS shells<sup>37</sup> and may result from scattering of strongly confined electrons in the shell by surface states and surface phonons<sup>38</sup> or inhomogeneity in faceting<sup>39</sup>. After complete conversion to HgSe through IE-CE, broadening fully disappears and the FWHM of HgSe products are as narrow as those of CdSe (Supplementary Table 4). Homogeneous  $Hg_xCd_{1-x}Se$  NCs exhibited a PL QY near 15–20% with a two-component exponential decay with half-times of 18.8 ns and 67.8 ns (Fig. 3j). In contrast, the CdSe–HgSe NCs exhibited a PL QY

below 1% and rapid PL decay. In addition, unlike  $Hg_xCd_{1-x}Se$  NCs, CdSe–HgSe NCs exhibit reduced PL QY with increasing NC size (Supplementary Fig. 8), an effect consistent with greater electron trapping by surface states in CdSe–HgSe, as expected from EMA calculations (Fig. 3e and Supplementary Fig. 9). As the NC size increases, the electron wavefunction in CdSe–HgSe becomes more localized to the shell, which reduces the 1S–1S electron–hole overlap integral (Supplementary Fig. 10) and is expected to reduce the absorption transition intensity and PL QY.

#### Mechanism of interdiffusion enhancement

The CE and IE-CE reactions differ primarily by the rates of Hg<sup>2+</sup>-Cd<sup>2+</sup> interdiffusion, based on fittings of a Fickian diffusion model to the NC composition over time (Supplementary Note 1)<sup>40</sup>. At 80 °C, IE-CE reaction dynamics fit well with a single  $Hg^{2+}$  diffusion coefficient (D) near 10<sup>-22</sup> m<sup>2</sup> s<sup>-1</sup> (Supplementary Fig. 11), indicating that the rate of surface CE and the interdiffusion rate are equivalent. However, the model fit was a poor match to experimental data for CE reactions, as the surface reaction rate is much faster than the interdiffusion rate. This was even the case when modelling Fickian diffusion only over the time course following rapid exchange of surface Cd2+ atoms, indicating that the exchange rate decreases with progressive replacement of Cd<sup>2+</sup> with Hg<sup>2+</sup>, creating stable CdSe-HgSe structures, which is consistent with a reaction occurring at temperatures well below the alloying temperature<sup>28</sup>. We could more precisely evaluate the time course of exchange with slower reactions at room temperature in the absence of alkylthiol ligands (Supplementary Fig. 12), conditions at which D was three orders of magnitude smaller, resulting in core-shell NCs both with and without the Ag enhancer. This allowed the observation that the initial burst of surface exchange was not impacted by Ag, which instead resulted in an approximately fourfold increase in D.

#### Role of Ag

Ag+diffuses in a CdSe lattice and occupies either interstitial sites (Ag<sub>i</sub>) or substitutional sites for cadmium  $(Ag_{Cd})^{26,41-43}$ . Two  $Ag_i$  sites together with a cation vacancy can form a charge-balanced 'Frenkel defect' that rapidly diffuses to enhance the interdiffusion of Cd<sup>2+</sup> and Hg<sup>2+</sup> across vacancies. This mechanism predicts a dependence of exchange rate on Ag concentration<sup>44,45</sup>, which we found to be true up to an amount of 0.075 Ag per Cd in a 3.3 nm CdSe NC (Supplementary Fig. 13). For this NC, we measured a mean 6.8 Ag incorporated per NC in Hg, Cd, Se intermediates, accounting for ~27% of the amount added (the remainder probably remained bound by ligands in solution). By a consideration of Poisson statistics, a mean of 6.8 Ag per NC corresponds to an NC distribution for which the vast majority of NCs (>99%) contain at least 2 Ag, the minimum number to form a Frenkel defect. This matches well to the expectation that fast, homogeneous exchange requires a Frenkel defect. Thus, when less Ag is added, a larger percentage of the NC population should contain fewer than 2 Ag, and experimentally, the exchange rate reduces and bands broadened (Supplementary Fig. 13), indicating a more heterogeneous reaction. With larger amounts of the Ag reagent, the CE rate also moderately decreased, PL bands broadened and low energy absorption tails appeared (Supplementary Fig. 14), an effect probably due to Ag<sub>Cd</sub> clusters that form mid-gap states<sup>46</sup>.

The capacity of Ag\* to catalyse Hg²+-Cd²+ interdiffusion was also consistent with experiments applying CdSe-HgSe NCs purified from excess ions after a CE reaction. When Ag was added to the CdSe-HgSe NCs at 80 °C, the absorption and emission spectra redshifted, the 1S-1S absorption band sharpened and strengthened, and the PL band narrowed and increased in QY (Fig. 4). There was no change in the absorption spectral features at energies well above the bandgap. These changes are consistent with interdiffusion-based shifts from a core-shell NC to a homogeneously alloyed NC without a change in overall composition. Because the PL spectra narrowed during alloying, the broadening of CdSe-HgSe NC spectra must not be a result of

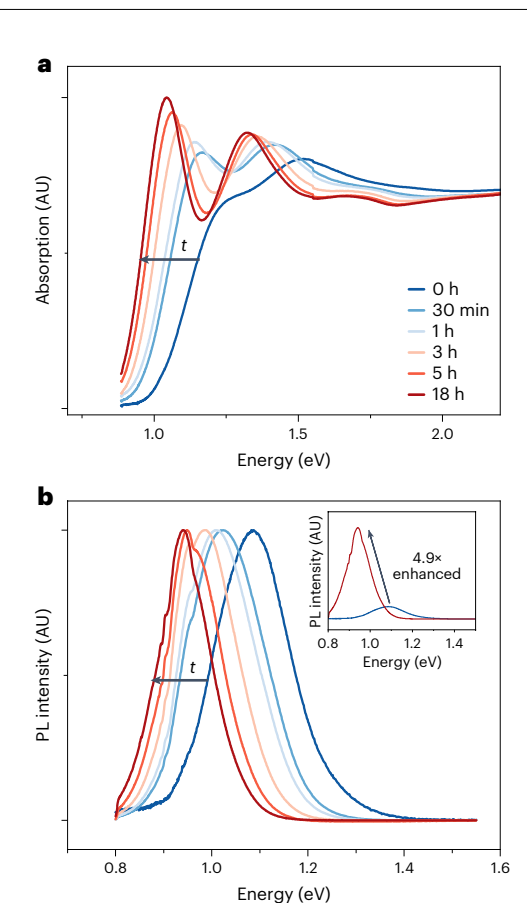


Fig. 4 | Interdiffusion-enhanced alloying of core-shell CdSe-HgSe NCs. After a CE reaction applying an excess of mercury, CdSe-HgSe NCs (composition  $x \approx 0.9$ ) were purified and reacted with the Ag reagent at 80 °C. a,b, The reaction time courses show changes in the absorption spectrum (a) and PL spectrum (b). Both spectra are normalized by the maximum intensity. The inset in b shows the PL spectra before and after the reaction normalized by QY.

population heterogeneity, indicating that CdSe–HgSe NCs intrinsically exhibit broader PL spectral bands than  $Hg_xCd_{1-x}Se$  NCs.

This IE-CE reaction on pre-formed CdSe-HgSe NCs did not occur if the NCs contained only a small amount of mercury that was insufficient to form a complete HgSe ML ( $x \approx 0.1$ ; Supplementary Fig. 15). This may be because the diffusion coefficient of Ag in mercury cadmium chalcogenide ternary alloys is enhanced by orders of magnitude when the alloys are mercury-rich, potentially arising from inter-mercury ion percolation chains 45,47. However, total Ag incorporation into NCs may also differ for NCs with different mercury content, as Ag content in the fully exchanged HgSe products was approximately half of that measured after partial exchange to Hg<sub>x</sub>Cd<sub>1-x</sub>Se NCs. This may partially explain why we were unable to use Ag-catalysed IE-CE to convert purified HgSe NCs to CdSe even in the presence of a large excess cadmium ions, although wider explorations of reaction conditions may make this possible. The chemical nature of the Ag dopant is thus complex and apparently changes as the NC transitions during IE-CE. X-ray spectroscopic methods may help to resolve these states<sup>42</sup>, although the extremely high Ag mobility<sup>45</sup> makes this challenging at temperatures relevant to the reaction.

#### Role of ligands

Strongly binding alkanethiol ligands (dodecanethiol, DDT) play an essential role in IE-CE as soft Lewis bases that coordinate soft  $Hg^{2+}$  and  $Ag^+$  cations on the NC surface and in solution. These ligands tune the surface exchange rate and are also required for the colloidal stability of  $Hg_{\nu}Cd_{1-\nu}Se$  NCs. An equivalent amount of -0.6-1.5 thiol per Cd in the

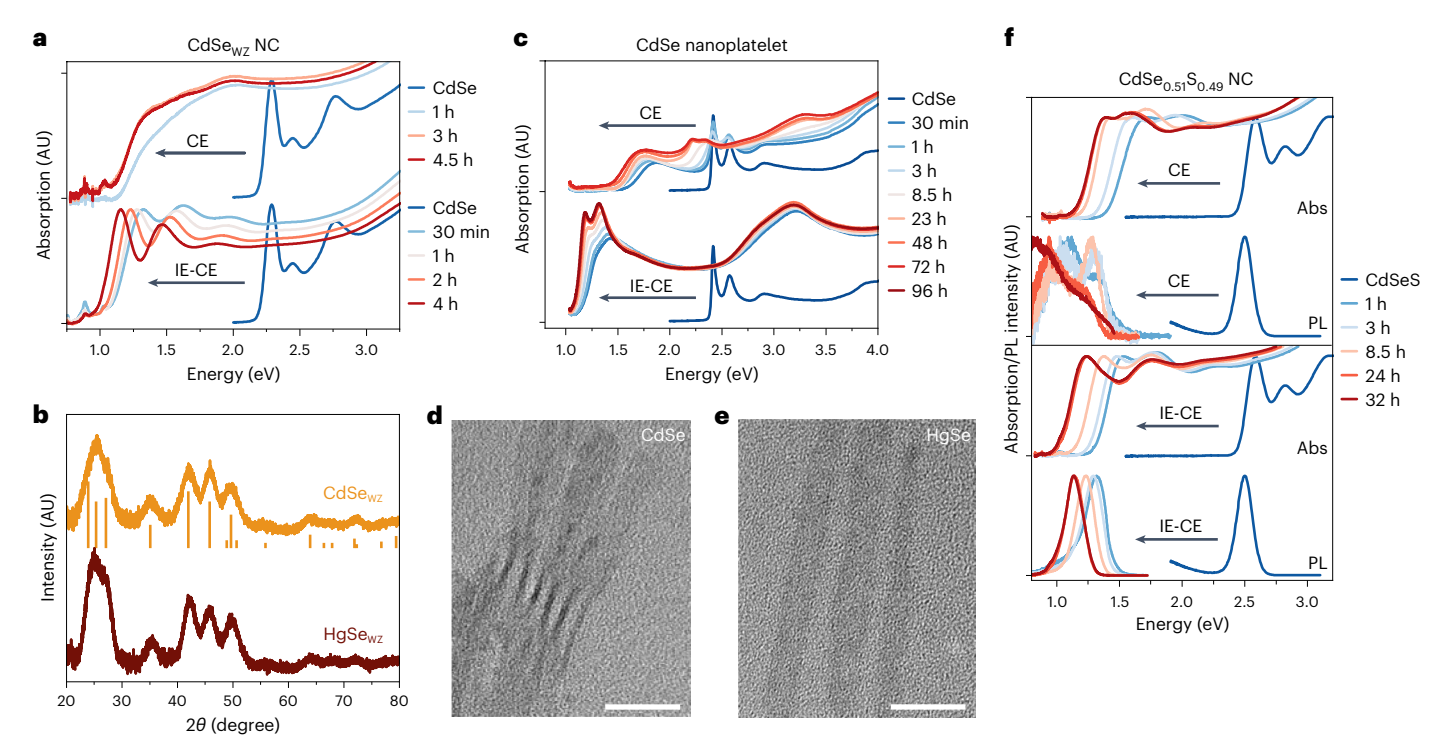


**Fig. 5** | **IE-CE on cores with different crystal structure, shape and composition. a**, Absorption spectra of wurtzite (WZ) CdSe NCs during CE (top) and IE-CE (bottom) normalized by the intensity of the IS-1S band. **b**, X-ray diffraction patterns of WZ CdSe NCs (orange) and their complete IE-CE products (brown). The vertical orange lines indicate bulk WZ CdSe. **c**, Absorption spectra of 4.5 ML CdSe nanoplatelet during CE (top) and IE-CE (bottom), normalized

by NC concentration. **d,e**, Transmission electron micrographs showing CdSe nanoplatelets (**d**) and their complete IE-CE products (**e**). Scale bars, 20 nm. **f**, Absorption and PL spectra of CdSe $_{0.51}$ S $_{0.49}$  NCs during CE (top) and IE-CE (bottom). The absorption and PL spectra are normalized by the maximum intensity of the 1S–1S band.

NC is optimal for homogeneous alloying when applying equivalents of 1.5 Hg and 0.075 Ag. This quantity of ligand is balanced to exceed the amount required to completely passivate the NC surface but is insufficient to coordinate Hg<sup>2+</sup> as unreactive dithiolate complexes. With increasing amounts of thiol, the exchange reaction decreases and almost no exchange reaction occurs in the presence of a large excess of the ligand (Supplementary Fig. 16). With low amounts of thiols insufficient to coordinate the NC surface, the absorption spectrum exhibits a weak 1S-1S transition and low PL OY similar to those of NCs exchanged without Ag, probably due to the fast surface reaction rate that yields a core-shell structure (Supplementary Fig. 16). However, after purification, the addition of thiol ligands increases the 1S-1S transition intensity and increases the PL QY more than 100-fold (Supplementary Fig. 17), indicating that thiols passivate the NC surface to prevent surface localized electrons from perturbation by surface states or surface phonons. Thiols further bind to Ag<sup>+</sup> in solution and reduce its reactivity to prevent heavy doping by Ag<sup>+</sup> (Supplementary Fig. 14). With the optimized amount of ligands, PL bandwidths are minimized and PL QY is maximized, and only a few Ag<sup>+</sup> per NC remain after exchange and can be easily extracted by the addition of trialkylphosphines (Supplementary Table 2).

#### Homogeneous alloying across phase, shape and composition

The IE-CE reaction can be applied to CdSe NCs with diverse structures to generate uniform HgSe and  $\mathrm{Hg_xCd_{1-x}}$ Se alloys that have not been generated through standard synthetic methods. The hexagonal wurtzite phase of CdSe NCs can be obtained through colloidal synthesis processes using ligands such as alkylphosphonic acids<sup>48</sup>. As with cubic phase CdSe NCs, CE reactions on wurtzite CdSe NCs halted after -3 h and absorption features resembled those of cubic CdSe–HgSe NCs (Fig. 5a), consistent with previous exchange reports<sup>49</sup>. These products exhibited much broader PL bands than their cubic counterparts (Supplementary Fig. 18), which may originate from the diverse facet

types on wurtzite NCs. In contrast, with IE-CE, complete conversion to HgSe occurred while the crystal structure was retained (Fig. 5b and Supplementary Table 5), yielding a non-natural crystal form that has not been synthesized in pure form previously to our knowledge. The bandgap energy of both cubic and wurtzite HgSe NCs with equal sizes were similar and both exhibited narrow PL bands.

Mercury exchange reactions with CdSe NPLs were performed at room temperature or below owing to the fragile morphology of these high surface area-to-volume ratio particles. As shown in Fig. 5c, CE reactions of 4.5-ML-thick CdSe NPLs resulted in an immediate redshift of absorption bands but with only small changes over the following 3 days. This has been observed previously<sup>27,35,50</sup> and indicates that the diffusion of Hg<sup>2+</sup> beyond  $2\,ML is hindered at room temperature. In contrast, the IE-CE process activates$ the diffusion of Hg<sup>2+</sup> below the surface layers such that the absorption spectrum at 30 min is more redshifted than that of the CE reaction after 3 days. As the reaction proceeds, two characteristic absorption peaks appear that are attributed to electronic transitions from heavy and light hole levels to the conduction band (Supplementary Fig. 19). Compared with the CdSe/ HgSe NPLs deriving from CE, absorption intensities of HgSe NPLs are several times larger, with 4.6-fold larger molar extinction coefficients at 3.1 eV (400 nm) compared with CdSe NPLs ( $\mu_{400}$  = 670,000 cm<sup>-1</sup>). Transmission electron microscopy revealed that the morphology was retained, and elemental analysis revealed that exchange was -98% complete and the original cation-to-anion ratio was maintained near 5:4 (Fig. 5d,e and Supplementary  $Table 6). CE\, reactions\, on\, CdSe_xS_{l-x} and\, CdTe\, NCs\, also\, accelerated\, with the\, Ag\,$ enhancer (Fig. 5f and Supplementary Fig. 20) and resulted in nearly completeexchange based on elemental analysis (Supplementary Table 5). In both cases, the PL bands became as narrow as those of the parent NCs. Similarly to the CE and IE-CE reactions using CdSe NCs, core-shell CdSe<sub>x</sub>S<sub>1-x</sub>-HgSe<sub>x</sub>S<sub>1-x</sub> NCs from CE reactions exhibited a much lower PL QY (<0.01%) than the homogeneous Cd<sub>v</sub>Hg<sub>1-v</sub>Se<sub>x</sub>S<sub>1-x</sub> and HgSe<sub>x</sub>S<sub>1-x</sub> NCs that resulted from IE-CE (PLQY-1-2%). From telluride to selenide to sulfide, the CE rate decreased in

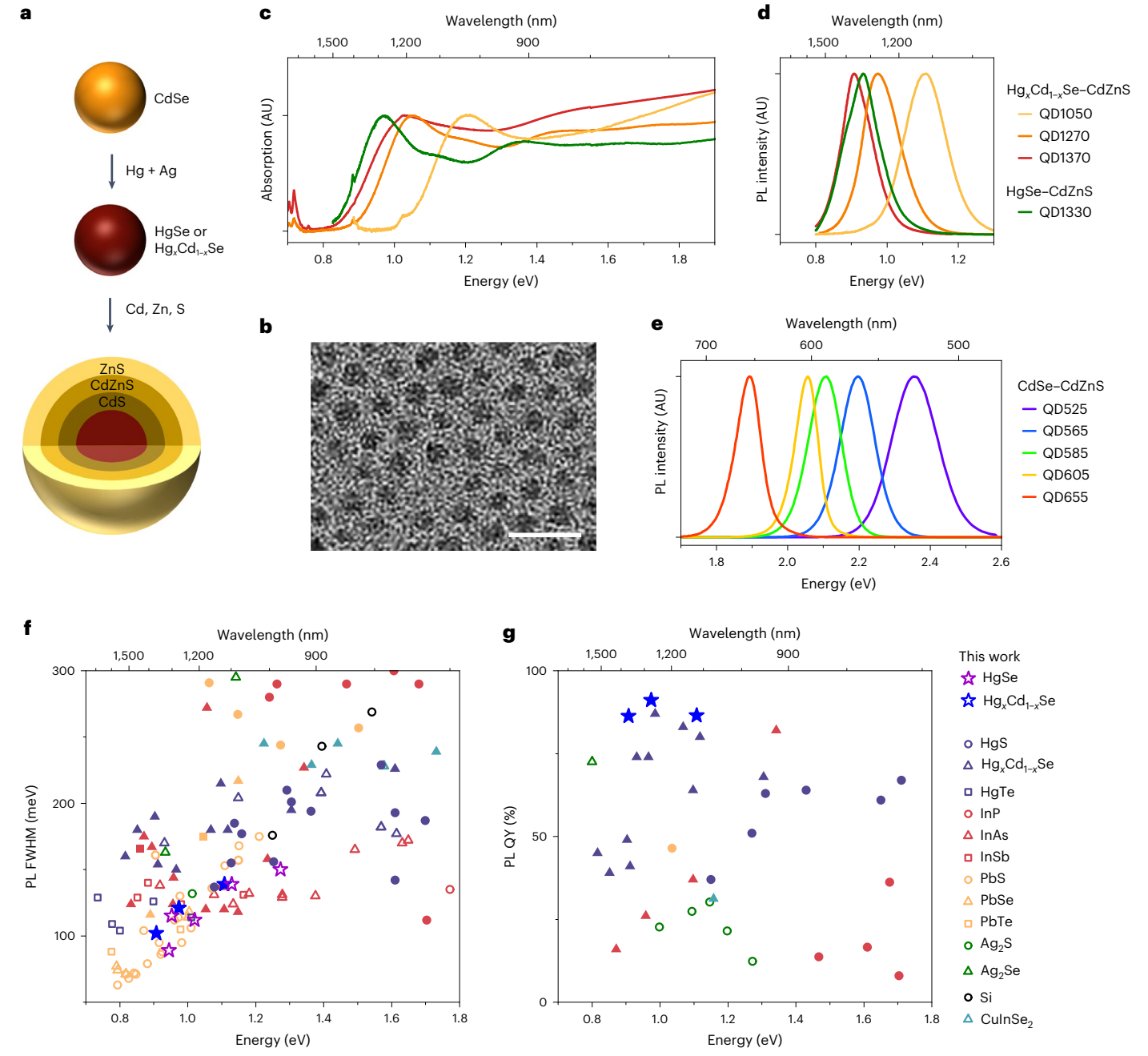


**Fig. 6** | **Characterization of core-shell HgSe-CdZnS and Hg\_xCd**<sub>1-x</sub>**Se-CdZnS NCs deriving from IE-CE. a**, Schematic representation of synthesis process. **b**, Transmission electron micrograph of  $Hg_xCd_{1-x}Se-CdZnS$  NCs (indicated as QD1270) with 3.2 nm core and shell composed of 0.8 ML CdS, 2.4 ML  $Cd_{0.5}Zn_{0.5}S$  and 0.8 ML of ZnS. Scale bar, 20 nm. An additional micrograph and size histogram are in Supplementary Fig. 23. **c**, Absorption spectra of four NCs with indicated structures. 1S-1S band energies are tuned by different degrees of CE. All cores are 3.2 nm, and shells are composed of 0.8 ML CdS, 2.4 ML  $Cd_{0.5}Zn_{0.5}S$  and 0.8 ML of ZnS. QDs are named by their PL band peak wavelength (such as 1,270 nm for

QD1270). **d**, PL spectra of four NCs with indicated structures. **e**, PL spectra of commercial visible spectrum CdSe–CdZnS NCs (Invitrogen) for comparison of bandwidths. **f**, PL FWHM values for  $Hg_x Cd_{1-x}Se$ , HgSe, HgSe–CdZnS and  $Hg_x Cd_{1-x}Se$ –CdZnS NCs (stars) in comparison with other core and core–shell NCs with PL between 700 and 1,700 nm wavelength reported in the literature. **g**, PL QY values for HgSe–CdZnS and  $Hg_x Cd_{1-x}Se$ –CdZnS NCs (stars) in comparison with other NCs with PL between 700 and 1,700 nm wavelength reported in the literature. The data are compiled in Supplementary Table 7. Open symbols in **f** and **g** indicate core NCs, and filled symbols indicate core–shell NCs.

accord with an increase in bond strength, probably slowing diffusion of Ag $^+$ . Complete conversion of CdTe NCs to HgTe NCs occurred through IE-CE at room temperature, whereas binary CdS NCs lacking selenium did not exhibit enhanced exchange with the Ag enhancer.

# Infrared emitting core-shell NCs

Towards the generation of high-QY emitters with PL in the infrared, we optimized the growth of insulating homovalent CdZnS shells on

HgSe and Hg<sub>x</sub>Cd<sub>1-x</sub>Se NCs prepared by IE-CE (Fig. 6a). As anticipated with the similar crystalline lattices of CdSe and HgSe, similar benefits of PL QY enhancement and PL bandwidth narrowing were observed for HgSe and Hg<sub>x</sub>Cd<sub>1-x</sub>Se cores as for CdSe cores after deposition of CdZnS shells <sup>38</sup>. Before shell growth, trioctylphosphine extraction of residual Ag<sup>+</sup> was needed to prevent the diffusion of Hg<sup>2+</sup> into the shell, which resulted in irreversible spectral blueshifts and broadening at elevated temperatures required for ZnS deposition (Supplementary Fig. 21).

With Ag<sup>+</sup> extraction, shell growth temperatures below -200 °C resulted in core—shell NCs with optical bandgaps slightly redshifted from those of the core (Fig. 6b,c and Supplementary Fig. 22), which similarly occurs for CdSe-based cores. After shell growth, the NC size increased from 3.2 nm to 6.0 nm (Fig. 6d and Supplementary Fig. 23) in agreement with the amount of shell precursors added. PL QY increased above 80%, and up to 91%, in the SWIR and the PL band narrowed to 102–139 meV FWHM (Fig. 6e, Supplementary Fig. 21 and Supplementary Table 5). Core–shell NCs based on HgSe NC cores exhibited the narrowest PL FWHMs, comparable to the most homogeneous PbS or PbSe NC cores and with comparable photophysical figures of merit as the commercial standards of visible spectrum NCs based on CdSe–CdZnS (Fig. 6e). PL energy bands were tuned by composition while keeping the NC core size fixed. PL FWHM and QY values are summarized in Fig. 6f,g in comparison with other infrared NCs reported so far (Supplementary Table 7) 9.11,2936,51-76.

#### Conclusion

In summary, we described a strategy to generate high-quality homogeneous binary and ternary NCs with infrared bandgaps. Using Ag enhancers with alkylthiol ligands, the cation interdiffusion rate and surface reaction rates can be balanced to achieve homogeneous mixing of cations across the NC. Unlike products with core-shell structures, the homogeneous alloys have enhanced exciton wavefunction overlap, which results in enhanced band edge absorbance and 1S-1S oscillator strength, high PL QY and narrow PL linewidths. After deposition of CdZnS shells, the NCs exhibited both brighter and narrower PL than previous mercury chalcogenide-based NCs and other colloidal semiconductor NCs in the SWIR window, which can be explained by the enhanced confinement of electron and hole wavefunctions in the NC core and matching lattice structure to the CdZnS shell. With the diversity of crystal phases, shapes and compositions now available in cadmium chalcogenides for applications in the visible spectrum, similar diversification of homogeneous and composition-tunable materials may now be readily obtainable in the infrared through IE-CE.

# Methods

# Chemicals

Cadmium acetate dihydrate (Cd(Ac)<sub>2</sub>·2H<sub>2</sub>O, 98%), cadmium oxide (CdO,  $\geq$ 99.99%), mercury acetate (Hg(Ac)<sub>2</sub>,  $\geq$ 99.0%), silver nitrate (AgNO<sub>3</sub>, >99%), sulfur (S, 99.98%), selenium (Se, 99.99%), tellurium (Te, 99.8%), selenium dioxide (SeO<sub>2</sub>, ≥99.9%), 1-octadecene (ODE, 90%), oleic acid (OLAc, 90%), oleylamine (OLAm, 70%) tetramethylammonium hydroxide (TMAH, 25 wt% in methanol), stearic acid (95%), trioctylphosphine oxide (TOPO, 99%), 1,2-hexadecanediol (HDD, 90%), diphenylphosphine (DPP, 98%), DDT ( $\geq$ 98%) and sodium hydroxide (NaOH,  $\geq$ 98%) were purchased from Sigma-Aldrich. N-tetradecylphosphonic acid (TDPA, >99%) was purchased from PCI Chemicals. Trioctylphosphine (TOP, 97%) was purchased from Strem Chemicals. Methanol (MeOH,  $\geq$ 99.8%) was purchased from Macron Fine Chemicals. Acetone (99.5%), chloroform (CHCl<sub>3</sub>, 99.8%), ethanol (EtOH, >95%), hexanes (98.5%), acetonitrile (99.9%) and toluene (99.5%) were purchased from Fisher Chemical. Myristic acid (99%) was purchased from Acros. Cadmium nitrate tetrahydrate (Cd(NO<sub>3</sub>)<sub>2</sub>·4H<sub>2</sub>O, 99.99%), zinc acetate (Zn(Ac)<sub>2</sub>, 99.98%), tetrachloroethylene (TCE, 99+%) and octadecylphosphonic acid (ODPA, 97%) were purchased from Alfa Aesar. All chemicals were used without further purification.

# Synthesis of precursors

For cadmium stearate  $(CdSt_2)$ ,  $Cd(Ac)_2 \cdot 2H_2O$  (5 mmol) was dissolved in MeOH (250 ml) in a 11 beaker. In a second 11 beaker, stearic acid (12.5 mmol) was dissolved in a mixture of 350 ml MeOH, 37.5 ml CHCl<sub>3</sub> and 5.25 ml of TMAH solution. The cadmium solution is added dropwise to the stearic acid solution using a dropping funnel. The product was isolated by vacuum filtration and washed several times with MeOH. For cadmium myristate  $(CdMy_2)^{77}$ , in a 11 beaker, NaOH (15 mmol) and myristic acid

 $(15 \, \text{mmol})$  were dissolved in MeOH  $(0.5 \, \text{l})$ . In a 100 ml beaker, CdNO<sub>3</sub>·4H<sub>2</sub>O  $(5 \, \text{mmol})$  was dissolved MeOH  $(50 \, \text{ml})$ . The cadmium solution was then added dropwise to the myristic acid solution with continuous stirring. The product was isolated by vacuum filtration and washed several times with MeOH. For Cd and Zn precursors for shell growth, Cd(Ac)<sub>2</sub> or Zn(Ac)<sub>2</sub>  $(1 \, \text{mmol})$  was dissolved in OLAm  $(10 \, \text{ml})$  at  $100 \, ^{\circ}\text{C}$ . For S precursor for shell growth, S powder  $(1 \, \text{mmol})$  was dissolved in ODE  $(10 \, \text{ml})$  at  $150 \, ^{\circ}\text{C}$ .

#### Synthesis of zinc blende CdSe NCs

In a 50 ml three-neck flask,  $CdSt_2$  (0.6 mmol),  $SeO_2$  (0.6 mmol), HDD (0.6 mmol) and ODE (15 ml) were added and dried under vacuum at 100 °C for 1 h. The solution was then rapidly heated to 230 °C under nitrogen at a rate of 20 °C min<sup>-1</sup> (to yield 3.2 nm CdSe NCs). The temperature was maintained for 15 min, and the reaction mixture was rapidly cooled by removing the heating mantle. At -110 °C, 3 ml of OLAc was injected to prevent precipitation of the NCs. The size was selected by controlling the reaction temperature and growth time. For purification, the crude solution is diluted with an equal volume of hexanes, and 1.5 ml of this solution is mixed with 35 ml MeOH and 5 ml acetone. After centrifugation, precipitates were dissolved in 1.5 ml hexanes. Precipitation with MeOH–acetone is repeated two more times before the products are finally dispersed in hexanes<sup>48</sup>.

#### Synthesis of wurtzite CdSe

CdO (60 mg), ODPA (280 mg) and TOPO (3.0 g) were added to a three-necked flask and heated to 300 °C under nitrogen until the solution became colourless and transparent. Then, TOP (1.5 g) was injected and the solution was heated to 380 °C. A selenium solution prepared by dissolving Se powder (58 mg) in TOP (360 mg) was injected into the cadmium solution, and the heating mantle was immediately removed. The NCs were diluted with toluene, precipitated twice with MeOH and finally dissolved in toluene.

# Synthesis of CdSe<sub>0.51</sub>S<sub>0.49</sub> NCs

CdO (0.2 mmol), stearic acid (0.6 mmol) and ODE (10 ml) were added to a three-necked flask and heated to 270 °C under nitrogen until the solution become coloirless and transparent. Then, a mixture of ODE-S (0.1 M, 0.5 ml) and Se suspended in ODE (0.1 M, 0.5 ml) was injected. After the injection, the temperature was set at 260 °C for 5 min. The NCs were purified using the same process used for zinc blende CdSe NCs.

#### Synthesis of CdTe NCs

CdO (12.8 mg, 0.1 mmol), TDPA (61 mg, 0.22 mmol) and ODE (5 ml) were added to a three-necked flask and heated under nitrogen to 300 °C until the solution became colourless and transparent. After cooling to room temperature, OLAm (0.5 ml) was added and the solution was heated to 300 °C under nitrogen. A tellurium solution was prepared by dissolving Te powder (12.76 mg, 0.1 mmol) in ODE (5 ml) and TOP (1 ml) at -280 °C. After cooling to room temperature, DPP (5  $\mu$ l) in OLAm (45  $\mu$ l) was added to the tellurium solution. The tellurium solution (3 ml) was then injected into the cadmium solution, and the temperature was set to 250 °C for 10 min. The reaction mixture was then cooled to room temperature, diluted with an equal volume of hexanes and centrifuged to remove unreacted white precursors. The NCs were purified by repeated extraction with hexane MeOH and finally dissolved in hexanes and stored at 4 °C under an inert atmosphere.

# Synthesis of 4.5 ML CdSe NPLs

In a 50 ml three-neck flask,  $Cd(My)_2$  (340 mg), Se (24 mg) and ODE (25 ml) were degassed for 30 min at room temperature. Under nitrogen flow, the temperature was then raised to 240 °C. When the mixture reached 220 °C,  $Cd(Ac)_2 \cdot 2H_2O$  (100 mg) was added and the reaction was stopped after 10 min at 240 °C. The NPLs were diluted with hexanes (30 ml) and precipitated with EtOH (30 ml). The NPLs were finally suspended in hexanes (10 ml).

#### **Mercury CE**

In a typical reaction, zinc blende CdSe NCs (100 nmol) dispersed in ODE (8 ml) were mixed with 100 equivalents of OLAm and 0.6–1.5 equivalents of DDT relative to the number of Cd ions in the NCs. A mercury precursor solution (0.1 M) was prepared by dissolving Hg(Ac2) in OLAm at 50 °C for 1 h. A silver precursor solution (0.02 M) was prepared by dissolving AgNO3 in OLAm by sonication at room temperature. The CdSe solution was heated to 80 °C, and a mixture of Hg and Ag precursor solutions was rapidly injected. Typically, 1.5 equivalents of Hg ions and 0.075 equivalents of Ag ions per Cd ions was used. The CE reaction was monitored by ultraviolet–visible–near-infrared absorption spectroscopy. The NCs were purified using the same process used for zinc blende CdSe NCs. The same protocol was used for CE of wurtzite CdSe NCs, CdSe $_{0.51}S_{0.49}$  NCs, CdTe NCs and CdSe NPLs with the exception that CdTe NCs and CdSe NPLs were reacted at room temperature and no thiol ligands were applied.

# Ag extraction

HgSe or  $Hg_xCd_{1-x}$ Se NCs (50 nmol) were dissolved in ODE (4 ml), OLAc (0.2 ml) and OLAm (0.1 ml). The solution was heated to 50 °C, and TOP (50 µl) was injected. After 2 h, NCs were purified twice and finally dissolved in hexanes. Before purification, the crude solution is diluted with an equal volume of hexanes and 1 ml of OLAc and OLAm is added to prevent the complete stripping of ligands during the purification. Then, 1.5 ml of this solution is mixed with 35 mL MeOH and 5 ml acetone for precipitation. After two times of precipitation, precipitates were dissolved in hexanes.

# Shell growth

For a typical reaction,  $Hg_xCd_{1-x}Se$  NCs (100 nmol) were dissolved in ODE (6 ml) and OLAm (2 ml) and heated to 50 °C. In all cases, shells were grown in 0.8 ML increments by dropwise addition of the S precursor followed by the Cd/Zn precursor. The growth of the first S layer was initiated at 50 °C. After 10 min, the NC solution was heated to 120 °C, and the Cd precursor was added and allowed to react for 10 min. The reaction temperature was raised in 10 °C increments between each precursor addition until reaching a maximum of 200 °C. Typically, 0.8 ML of CdS, 2.4 ML of  $Cd_{0.5}Zn_{0.5}S$  and 0.8 ML of ZnS were successively overcoated. After the reaction, NCs were purified by precipitation with MeOH and acetone three times and finally dispersed in hexanes.

# Instrumentation

TEM images and EDS data were obtained using a JEOL JEM-2100F and JEOL 2010 LaB6. Powder X-ray diffraction patterns were obtained using a Bruker D8 ADVANCE. ICP-OES was performed using a PerkinElmer Optima 8300. Absorption spectra were obtained using an Agilent Cary 5000 UV-Vis-NIR spectrophotometer. PL spectra were obtained using a Horiba NanoLog fluorometer. PL lifetime was measured at room temperature with a home-built single-photon-counting spectroscopy setup at the Materials Research Laboratory at UIUC.

# Spectral decomposition and oscillator strength calculations

A Gaussian mixture model was fit to energy-scaled absorption spectra, A(E), obtained from NC suspensions with experimentally measured concentration and diameter as previously described<sup>34</sup>, with

$$A(E) = \sum_{i=1}^{n} \frac{a_i}{2\sqrt{2\pi} dR(E_i - E_g)} \exp\left[-\frac{(E - E_g)^2}{8dR^2(E_i - E_g)^2}\right],$$
 (1)

where each Gaussian function  $\frac{1}{i}$  has area  $a_i$  and centroid energy  $E_i$ , dR is the relative standard deviation of NC radius and  $E_g$  is the bulk bandgap energy. To calculate  $E_g$  for CdSe–HgSe and Hg<sub>x</sub>Cd<sub>1-x</sub>Se, a linear interpolation between the bandgaps of CdSe (1.74 eV) and HgSe (-0.06 eV) was applied on the basis of the total NC composition x. The values  $a_i$ ,  $E_i$  and

dR were fitting parameters with initial guesses for  $E_i$  and the number of transitions n determined from minima of the second derivative of A (E).  $E_i$  values were fixed within  $\pm 50$  meV of initial guesses, while  $a_i$  and dR were unbounded. The models were fit using the least squares method in Matlab. The values of  $a_i$  were proportional to oscillator strength when the NC size is fixed  $^{34}$ , and only relative values were determined.

#### **EMA calculations**

NCs were modelled as spherically symmetric concentric layers with finite potential energy for non-interacting electrons and holes by the method of Haus et al. 78 and described further for the CdTe-HgTe and Hg, Cd<sub>1-x</sub>Te systems by Smith et al.<sup>34</sup> The time-independent Schrödinger equation in three dimensions was solved to calculate the kinetic energies and normalized wavefunctions of the electron  $(\psi_a)$  and hole  $(\psi_b)$ , and the bandgap energy was calculated with inclusion of a Coulombic term as a perturbation. For Hg<sub>x</sub>Cd<sub>1-x</sub>Se alloy domains, a linear interpolation between materials parameters of CdSe and HgSe was applied on the basis of the NC composition x, including for the electron effective masses  $(m_{\rm e,CdSe}=0.112,m_{\rm e,HgSe}=0.042)$ , hole effective masses  $(m_{\rm h,CdSe}=0.469,$  $m_{\rm h,HgSe} = 0.019$ ), dielectric constants ( $\varepsilon_{\infty,CdSe} = 6.2$ ,  $\varepsilon_{\infty,HgSe} = 16.5$ ), electronic bandgaps, conduction band offsets ( $\Delta E_{C.C.dSe} = -1.36 \, \text{eV}$ ,  $\Delta E_{\text{C,HgSe}} = -2.69 \,\text{eV}$ ), valence band offsets ( $\Delta E_{\text{V,CdSe}} = 0.60 \,\text{eV}$ ,  $\Delta E_{V,HgSe} = 1.07 \text{ eV}$ ) and cubic lattice parameters  $a_c$ . The total wavefunction overlap  $\phi_{total}$  was calculated as

$$\phi_{\text{total}} = \int_{0}^{\infty} 4\pi r^{2} \psi_{e} \psi_{h} dr, \qquad (2)$$

where r is the radial distance from the NC centre. The surface electronic wavefunction localization  $\phi_{e, \text{surf}}$  was calculated as the integrated radial distribution function starting from approximately one atomic layer from the surface of a NC with radius  $r_{\text{NC}}$  as

$$\phi_{e,\text{surf}} = \int_{r_{\text{NC}} - a_c/4}^{\infty} 4\pi r^2 \psi_e^2 dr.$$
 (3)

#### **PL QY calculations**

For QY measurements, NCs were dispersed in TCE and diluted so that the absorption was -0.05 at 700 nm. Relative QY was measured with respect to indocyanine green (in DMSO, QY of 13%) under 700 nm excitation.

#### **Absorption coefficient calculations**

The molar absorption coefficients of CdSe NCs were calculated on the basis of the reported correlations between the size and 1S–1S band energy. The molar absorption coefficient of  $Hg_xCd_{1-x}Se$  NCs and  $Hg_xCd_{1-x}Se$ –CdZnS NCs were calculated by assuming the number of NCs did not change during the IE-CE reaction and shell overcoating process. The intrinsic absorption coefficient ( $\mu$ ) was derived from the absorbance (A) of the NC solution as

$$\mu = \frac{\ln(10)A}{f_{V}L},\tag{4}$$

where  $f_V$  is the volume fraction of NCs in solution and L is the optical path length of the cuvette (1 cm).

# Data availability

All relevant data are provided within this paper and Supplementary Information.

#### References

 García de Arquer, F. P. et al. Semiconductor quantum dots: technological progress and future challenges. Science 373, eaaz8541 (2021).

Nature Synthesis

- Murray, C. B., Norris, D. J. & Bawendi, M. G. Synthesis and characterization of nearly monodisperse CdE (E = sulfur, selenium, tellurium) semiconductor nanocrystallites. *J. Am. Chem. Soc.* 115, 8706–8715 (1993).
- Kim, J. Y., Voznyy, O., Zhitomirsky, D. & Sargent, E. H. 25th Anniversary Article: colloidal quantum dot materials and devices: a quarter-century of advances. Adv. Mater. 25, 4986–5010 (2013).
- Pietryga, J. M. et al. Spectroscopic and device aspects of nanocrystal quantum dots. Chem. Rev. 116, 10513-10622 (2016).
- 5. Jang, E. & Jang, H. Review: quantum dot light-emitting diodes. *Chem. Rev.* **123**, 4663–4692 (2023).
- Park, J., Jayaraman, A., Schrader, A. W., Hwang, G. W. & Han, H.-S. Controllable modulation of precursor reactivity using chemical additives for systematic synthesis of high-quality quantum dots. *Nat. Commun.* 11, 5748 (2020).
- Vasilopoulou, M. et al. Advances in solution-processed near-infrared light-emitting diodes. Nat. Photonics 15, 656-669 (2021).
- 8. Yang, Y., Jiang, Q. & Zhang, F. Nanocrystals for deep-tissue in vivo luminescence imaging in the near-infrared region. *Chem. Rev.* **124**, 554–628 (2024).
- Franke, D. et al. Continuous injection synthesis of indium arsenide quantum dots emissive in the short-wavelength infrared. *Nat.* Commun. 7, 12749 (2016).
- Janke, E. M. et al. Origin of broad emission spectra in InP quantum dots: contributions from structural and electronic disorder. *J. Am. Chem.* Soc. **140**, 15791–15803 (2018).
- Hendricks, M. P., Campos, M. P., Cleveland, G. T., Jen-La Plante, I. & Owen, J. S. A tunable library of substituted thiourea precursors to metal sulfide nanocrystals. Science 348, 1226–1230 (2015).
- Campos, M. P. et al. A library of selenourea precursors to PbSe nanocrystals with size distributions near the homogeneous limit. J. Am. Chem. Soc. 139, 2296–2305 (2017).
- Peng, X. et al. In situ TEM study of the degradation of PbSe nanocrystals in air. Chem. Mater. 31, 190–199 (2019).
- Beygi, H., Sajjadi, S. A., Babakhani, A., Young, J. F. & van Veggel, F.
  C. J. M. Surface chemistry of as-synthesized and air-oxidized PbS quantum dots. Appl. Surf. Sci. 457, 1–10 (2018).
- Gréboval, C. et al. Mercury chalcogenide quantum dots: material perspective for device integration. *Chem. Rev.* 121, 3627–3700 (2021).
- Lu, H., Carroll, G. M., Neale, N. R. & Beard, M. C. Infrared quantum dots: progress, challenges, and opportunities. ACS Nano 13, 939–953 (2019).
- Deng, Z., Jeong, K. S. & Guyot-Sionnest, P. Colloidal quantum dots intraband photodetectors. ACS Nano 8, 11707–11714 (2014).
- Kamath, A., Melnychuk, C. & Guyot-Sionnest, P. Toward bright mid-infrared emitters: thick-shell n-type HgSe/CdS nanocrystals. J. Am. Chem. Soc. 143, 19567–19575 (2021).
- Kamath, A., Schaller, R. D. & Guyot-Sionnest, P. Bright fluorophores in the second near-infrared window: HgSe/CdSe quantum dots. J. Am. Chem. Soc. 145, 10809–10816 (2023).
- Madejczyk, P., Manyk, T. & Rutkowski, J. Research on electro-optical characteristics of infrared detectors with HgCdTe operating at room temperature. Sensors 23, 1088 (2023).
- Smith, A. M. & Nie, S. Bright and compact alloyed quantum dots with broadly tunable near-infrared absorption and fluorescence spectra through mercury cation exchange. J. Am. Chem. Soc. 133, 24–26 (2011).
- De Trizio, L. & Manna, L. Forging colloidal nanostructures via cation exchange reactions. Chem. Rev. 116, 10852–10887 (2016).
- 23. Groeneveld, E. et al. Tailoring ZnSe–CdSe colloidal quantum dots via cation exchange: from core/shell to alloy nanocrystals. *ACS Nano* **7**, 7913–7930 (2013).
- Koscher, B. A., Bronstein, N. D., Olshansky, J. H., Bekenstein, Y. & Alivisatos, A. P. Surface- vs diffusion-limited mechanisms of anion

- exchange in CsPbBr<sub>3</sub> nanocrystal cubes revealed through kinetic studies. *J. Am. Chem. Soc.* **138**, 12065–12068 (2016).
- Ma, F., Abboud, K. A. & Zeng, C. Precision synthesis of a CdSe semiconductor nanocluster via cation exchange. *Nat. Synth.* 2, 949–959 (2023).
- 26. Dutt, M. & Sharma, B. in Diffusion in Semiconductors 1–63 (1998).
- 27. Izquierdo, E. et al. Strongly confined HgTe 2D nanoplatelets as narrow near-infrared emitters. *J. Am. Chem.* Soc. **138**, 10496–10501 (2016).
- 28. Shen, G. & Guyot-Sionnest, P. HgTe/CdTe and HgSe/CdX (X = S, Se, and Te) core/shell mid-infrared quantum dots. *Chem. Mater.* **31**, 286–293 (2019).
- Sarkar, S. et al. Short-wave infrared quantum dots with compact sizes as molecular probes for fluorescence microscopy. J. Am. Chem. Soc. 142, 3449–3462 (2020).
- 30. Choi, D. et al. Major electronic transition shift from bandgap to localized surface plasmon resonance in Cd<sub>x</sub>Hg<sub>1-x</sub>Se alloy nanocrystals. *Chem. Mater.* **29**, 8548–8554 (2017).
- 31. Moreels, I. et al. Size-dependent optical properties of colloidal PbS quantum dots. ACS Nano 3, 3023–3030 (2009).
- Moreels, I. et al. Composition and size-dependent extinction coefficient of colloidal PbSe quantum dots. Chem. Mater. 19, 6101–6106 (2007).
- 33. Massiot, I., Cattoni, A. & Collin, S. Progress and prospects for ultrathin solar cells. *Nat. Energy* **5**, 959–972 (2020).
- Smith, A. M., Lane, L. A. & Nie, S. Mapping the spatial distribution of charge carriers in quantum-confined heterostructures. *Nat. Commun.* 5, 4506 (2014).
- 35. Izquierdo, E. et al. Coupled HgSe colloidal quantum wells through a tunable barrier: a strategy to uncouple optical and transport band gap. *Chem. Mater.* **30**, 4065–4072 (2018).
- Lee, G. et al. Design and synthesis of CdHgSe/HgS/CdZnS core/multi-shell quantum dots exhibiting high-quantum-yield tissue-penetrating shortwave infrared luminescence. Small 19, 2301161 (2023).
- Sayevich, V. et al. Highly versatile near-infrared emitters based on an atomically defined HgS interlayer embedded into a CdSe/CdS quantum dot. Nat. Nanotechnol. 16, 673–679 (2021).
- Cui, J. et al. Evolution of the single-nanocrystal photoluminescence linewidth with size and shell: implications for exciton-phonon coupling and the optimization of spectral linewidths. *Nano Lett.* 16, 289–296 (2016).
- 39. Nguyen, H. A. et al. Design rules for obtaining narrow luminescence from semiconductors made in solution. *Chem. Rev.* **123**, 7890–7952 (2023).
- Gupta, A. et al. Diffusion-limited kinetics of isovalent cation exchange in III–V nanocrystals dispersed in molten salt reaction media. Nano Lett. 22, 6545–6552 (2022).
- 41. Sahu, A. et al. Electronic impurity doping in CdSe nanocrystals. *Nano Lett.* **12**, 2587–2594 (2012).
- 42. Ott, F. D., Spiegel, L. L., Norris, D. J. & Erwin, S. C. Microscopic theory of cation exchange in CdSe nanocrystals. *Phys. Rev. Lett.* **113**, 156803 (2014).
- 43. Kompch, A. et al. Localization of Ag dopant atoms in CdSe nanocrystals by reverse Monte Carlo analysis of EXAFS spectra. *J. Phys. Chem. C* **119**, 18762–18772 (2015).
- Casavola, M. et al. Anisotropic cation exchange in PbSe/CdSe core/shell nanocrystals of different geometry. *Chem. Mater.* 24, 294–302 (2012).
- Cahen, D. & Lubomirsky, I. Percolation-controlled semiconductor doping. Chem. Mater. 10, 2596–2598 (1998).
- Yang, L. et al. One-pot synthesis of monodisperse colloidal copper-doped CdSe nanocrystals mediated by ligand-copper interactions. Chem. Mater. 28, 7375–7384 (2016).

- Lyubomirsky, I., Lyakhovitskaya, V., Triboulet, R. & Cahen,
  D. Substitutional-interstitial silver diffusion and drift in bulk (cadmium,mercury) telluride: results and mechanistic implications. J. Electron. Mater. 26, 97–105 (1997).
- Carbone, L. et al. Synthesis and micrometer-scale assembly of colloidal CdSe/CdS nanorods prepared by a seeded growth approach. Nano Lett. 7, 2942–2950 (2007).
- Dumett Torres, D., Banerjee, P., Pamidighantam, S. & Jain, P. K. A non-natural wurtzite polymorph of HgSe: a potential 3D topological insulator. Chem. Mater. 29, 6356–6366 (2017).
- Dabard, C. et al. Optimized cation exchange for mercury chalcogenide 2D nanoplatelets and its application for alloys. Chem. Mater. 33, 9252–9261 (2021).
- 51. Yadav, R. et al. Narrow near-infrared emission from InP QDs synthesized with indium(I) halides and aminophosphine. *J. Am. Chem.* Soc. **145**, 5970–5981 (2023).
- 52. Dennis, A. M. et al. Suppressed blinking and Auger recombination in near-infrared type-II InP/CdS nanocrystal quantum dots. *Nano Lett.* **12**, 5545–5551 (2012).
- Saeboe, A. M. et al. Extending the near-infrared emission range of indium phosphide quantum dots for multiplexed in vivo imaging. *Nano Lett.* 21, 3271–3279 (2021).
- Srivastava, V., Dunietz, E., Kamysbayev, V., Anderson, J. S. & Talapin, D. V. Monodisperse InAs quantum dots from aminoarsine precursors: understanding the role of reducing agent. *Chem. Mater.* 30, 3623–3627 (2018).
- Srivastava, V., Janke, E. M., Diroll, B. T., Schaller, R. D. & Talapin, D. V. Facile, economic and size-tunable synthesis of metal arsenide nanocrystals. *Chem. Mater.* 28, 6797–6802 (2016).
- Ginterseder, M. et al. Scalable synthesis of InAs quantum dots mediated through indium redox chemistry. J. Am. Chem. Soc. 142, 4088–4092 (2020).
- Liu, W., Chang, A. Y., Schaller, R. D. & Talapin, D. V. Colloidal InSb nanocrystals. J. Am. Chem. Soc. 134, 20258–20261 (2012).
- Busatto, S. et al. Luminescent colloidal InSb quantum dots from in situ generated single-source precursor. ACS Nano 14, 13146–13160 (2020).
- Weidman, M. C., Beck, M. E., Hoffman, R. S., Prins, F. & Tisdale,
  W. A. Monodisperse, air-stable PbS nanocrystals via precursor stoichiometry control. ACS Nano 8, 6363–6371 (2014).
- Pietryga, J. M. et al. Utilizing the lability of lead selenide to produce heterostructured nanocrystals with bright, stable infrared emission. J. Am. Chem. Soc. 130, 4879–4885 (2008).
- Kovalenko, M. V., Schaller, R. D., Jarzab, D., Loi, M. A. & Talapin, D. V. Inorganically functionalized PbS–CdS colloidal nanocrystals: integration into amorphous chalcogenide glass and luminescent properties. *J. Am. Chem.* Soc. **134**, 2457–2460 (2012).
- Kovalenko, M. V. et al. Quasi-seeded growth of ligand-tailored PbSe nanocrystals through cation-exchange-mediated nucleation. *Angew. Chem.* 120, 3071–3075 (2008).
- Yu, W. W., Falkner, J. C., Shih, B. S. & Colvin, V. L. Preparation and characterization of monodisperse PbSe semiconductor nanocrystals in a noncoordinating solvent. *Chem. Mater.* 16, 3318–3322 (2004).
- 64. Abel, K. A., Qiao, H., Young, J. F. & van Veggel, F. C. J. M. Four-fold enhancement of the activation energy for nonradiative decay of excitons in PbSe/CdSe core/shell versus PbSe colloidal quantum dots. *J. Phys. Chem. Lett.* **1**, 2334–2338 (2010).
- Murphy, J. E. et al. PbTe colloidal nanocrystals: synthesis, characterization, and multiple exciton generation. *J. Am. Chem.* Soc. 128, 3241–3247 (2006).
- Protesescu, L., Zünd, T., Bodnarchuk, M. I. & Kovalenko, M. V. Air-stable, near- to mid-infrared emitting solids of PbTe/CdTe core–shell colloidal quantum dots. *ChemPhysChem* 17, 670–674 (2016).

- 67. Sung, Y., Lee, W., Lee, E., Ko, Y. H. & Kim, S. Ion-pair ligand-assisted surface stoichiometry control of Ag<sub>2</sub>S nanocrystals. *Chem. Mater.* **34.** 9945–9954 (2022).
- 68. He, H. et al. Ultrasmall Pb: $Ag_2S$  quantum dots with uniform particle size and bright tunable fluorescence in the NIR-II window. Small **14**, 1703296 (2018).
- 69. Zhu, C.-N. et al. Ag<sub>2</sub>Se quantum dots with tunable emission in the second near-infrared window. *ACS Appl. Mater. Interfaces* **5**, 1186–1189 (2013).
- 70. Ding, Q. et al. Enantiomeric NIR-II emitting rare-earth-doped Ag₂Se nanoparticles with differentiated in vivo imaging efficiencies. *Angew. Chem.* **134**, e202210370 (2022).
- 71. Wheeler, L. M. et al. Silyl radical abstraction in the functionalization of plasma-synthesized silicon nanocrystals. *Chem. Mater.* **27**, 6869–6878 (2015).
- 72. Cassette, E. et al. Synthesis and characterization of near-infrared Cu–In–Se/ZnS core/shell quantum dots for in vivo imaging. *Chem. Mater.* **22**, 6117–6124 (2010).
- 73. Li, Y. et al. Bright, magnetic NIR-II quantum dot probe for sensitive dual-modality imaging and intensive combination therapy of cancer. ACS Nano 16, 8076–8094 (2022).
- 74. Mews, A., Eychmueller, A., Giersig, M., Schooss, D. & Weller, H. Preparation, characterization, and photophysics of the quantum dot quantum well system cadmium sulfide/mercury sulfide/cadmium sulfide. *J. Phys. Chem.* **98**, 934–941 (1994).
- Kovalenko, M. V. et al. Colloidal HgTe nanocrystals with widely tunable narrow band gap energies: from telecommunications to molecular vibrations. J. Am. Chem. Soc. 128, 3516–3517 (2006).
- 76. Kershaw, S. V., Yiu, W. K., Sergeev, A. & Rogach, A. L. Development of synthetic methods to grow long-wavelength infrared-emitting HgTe quantum dots in dimethylformamide. *Chem. Mater.* **32**, 3930–3943 (2020).
- 77. Cho, W. et al. Direct synthesis of six-monolayer (1.9 nm) thick zinc-blende CdSe nanoplatelets emitting at 585 nm. *Chem. Mater.* **30**, 6957–6960 (2018).
- Haus, J. W., Zhou, H. S., Honma, I. & Komiyama, H. Quantum confinement in semiconductor heterostructure nanometer-size particles. *Phys. Rev. B* 47, 1359–1365 (1993).

#### Acknowledgements

This work was supported by funds from the National Institutes of Health (R01CA227699, R01GM131272, R01EB032249 and R01EB032725 to A.M.S.) and the National Science Foundation (2232681 to A.M.S.).

# **Author contributions**

W.L. and A.M.S. conceived and designed the experiments, characterizations and modelling, and contributed to the theory. W.L. performed all chemical syntheses and optical characterizations. A.M.S. modelled the band structure using EMA. W.L. and A.M.S. wrote the paper.

# **Competing interests**

The authors declare no competing interests.

#### **Additional information**

**Supplementary information** The online version contains supplementary material available at https://doi.org/10.1038/s44160-024-00597-3.

 $\begin{tabular}{ll} \textbf{Correspondence and requests for materials} should be addressed to Andrew M. Smith. \end{tabular}$ 

**Peer review information** *Nature Synthesis* thanks Peter Reiss and the other, anonymous, reviewer(s) for their contribution to the

peer review of this work. Primary Handling Editor: Alexandra Groves, in collaboration with the *Nature Synthesis* team.

**Reprints and permissions information** is available at www.nature.com/reprints.

**Publisher's note** Springer Nature remains neutral with regard to jurisdictional claims in published maps and institutional affiliations.

Springer Nature or its licensor (e.g. a society or other partner) holds exclusive rights to this article under a publishing agreement with the author(s) or other rightsholder(s); author self-archiving of the accepted manuscript version of this article is solely governed by the terms of such publishing agreement and applicable law.

@ The Author(s), under exclusive licence to Springer Nature Limited 2024

# **QUERY FORM**

<b>Manuscript ID</b>	[Art. ld: 597]	
Author	Wonseok Lee	

# **AUTHOR:**

The following queries have arisen during the editing of your manuscript. Please answer by making the requisite corrections directly in the e.proofing tool rather than marking them up on the PDF. This will ensure that your corrections are incorporated accurately and that your paper is published as quickly as possible.

Query No.	Nature of Query
Q1:	Throughout the paper, please confirm the replacement of the forward slash in core/shell structures with an en dash to signify the combination, per style.
Q2:	Please check your article carefully, coordinate with any co-authors and enter all final edits clearly in the eproof, remembering to save frequently. Once corrections are submitted, we cannot routinely make further changes to the article.
Q3:	Note that the eproof should be amended in only one browser window at any one time; otherwise changes will be overwritten.
Q4:	Author surnames have been highlighted. Please check these carefully and adjust if the first name or surname is marked up incorrectly, as this will affect indexing of your article in public repositories such as PubMed. Also, carefully check the spelling and numbering of all author names and affiliations, and the corresponding author(s) email address(es). Please note that email addresses should only be included for designated corresponding authors, and you cannot change corresponding authors at this stage except to correct errors made during typesetting.
Q5:	You cannot alter accepted Supplementary Information files except for critical changes to scientific content. If you do resupply any files, please also provide a brief (but complete) list of changes. If these are not considered scientific changes, any altered Supplementary files will not be used, only the originally accepted version will be published.
Q6:	Please check Figures for accuracy as they have been relabelled. Please markup minor changes in the eProof. For major changes, please provide revised figures. (Please note that in the eProof the figure resolution will appear at lower resolution than in the pdf and html versions of your paper.)
Q7:	If applicable, please ensure that any accession codes and datasets whose DOIs or other identifiers are mentioned in the paper are scheduled for public release as soon as possible, we recommend within a few days of submitting your proof, and update the database record with publication details from this article once available.
Q8:	In Fig. 2 caption, please clarify the difference between panels d and e.

# **QUERY FORM**

Manuscript ID	[Art. Id: 597]
Author	Wonseok Lee

# **AUTHOR:**

The following queries have arisen during the editing of your manuscript. Please answer by making the requisite corrections directly in the e.proofing tool rather than marking them up on the PDF. This will ensure that your corrections are incorporated accurately and that your paper is published as quickly as possible.

Query No.	Nature of Query	
Q9:	In the sentence beginning 'As the NC size increases, the…', please confirm the change has retained the intended meaning.	
Q10:	In Fig. 6 caption, in the sentence beginning 'An additional micrograph and', please confirm the change has retained the intended meaning.	
Q11:	In the sentence beginning 'The NCs were purified by', please confirm the change has retained the intended meaning.	
Q12:	In the sentence beginning 'ICP-OES was performed …', please expand ICP-OES.	
Q13:	In the sentence beginning 'PL lifetime was measured at…', please expand UIUC.	
Q14:	Please confirm the presentation of the equations and variables in this paper is ok, or revise where necessary.	
Q15:	For ref. 26, please add publisher, and editor(s) if appropriate.	